Design and Structural Optimization of Topological Interlocking Assemblies

ZIQI WANG, EPFL
PENG SONG, EPFL, Singapore University of Technology and Design
FLORIN ISVORANU, EPFL
MARK PAULY, EPFL

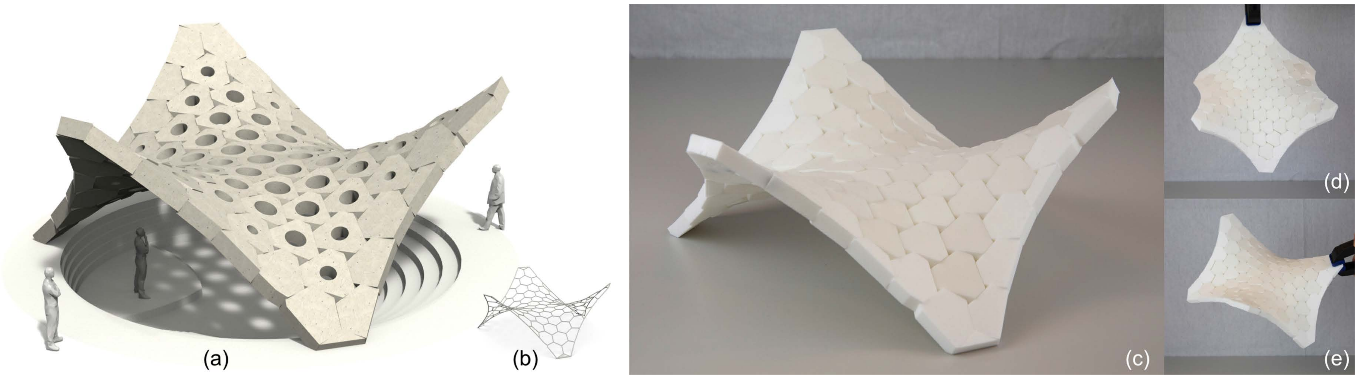

Fig. 1. A topological interlocking assembly (a) designed with our approach to conform to an input freeform design surface (b). The 3D printed prototype (c-e) is stable under different orientations.

We study assemblies of convex rigid blocks regularly arranged to approximate a given freeform surface. Our designs rely solely on the geometric arrangement of blocks to form a stable assembly, neither requiring explicit connectors or complex joints, nor relying on friction between blocks. The convexity of the blocks simplifies fabrication, as they can be easily cut from different materials such as stone, wood, or foam. However, designing stable assemblies is challenging, since adjacent pairs of blocks are restricted in their relative motion only in the direction orthogonal to a single common planar interface surface. We show that despite this weak interaction, structurally stable, and in some cases, globally interlocking assemblies can be found for a variety of freeform designs. Our optimization algorithm is based on a theoretical link between static equilibrium conditions and a geometric, global interlocking property of the assembly—that an assembly is globally interlocking if and only if the equilibrium conditions are satisfied for arbitrary external forces and torques. Inspired by this connection, we define a measure of stability that spans from single-load equilibrium to global interlocking, motivated by tilt analysis experiments used in structural engineering. We use this measure to optimize the geometry of blocks to achieve a static equilibrium for a maximal cone of directions, as opposed to considering only self-load scenarios with a single gravity direction. In the limit, this optimization can achieve globally interlocking structures. We show how different geometric patterns give rise to a variety of design options and validate our results with physical prototypes.

CCS Concepts: • **Computing methodologies** → *Shape modeling*; • **Applied computing** → *Computer-aided manufacturing*.

Additional Key Words and Phrases: 3D assembly, topological interlocking, equilibrium, stability analysis, computational design, structural optimization

ACM Reference Format:
Ziqi Wang, Peng Song, Florin Isvoranu, and Mark Pauly. 2019. Design and Structural Optimization of Topological Interlocking Assemblies. *ACM Trans. Graph.* 38, 6, Article 193 (November 2019), 13 pages. https://doi.org/10.1145/3355089.3356489

1 INTRODUCTION

This paper is about assemblies of convex rigid blocks. More specifically, we study how an ensemble of convex blocks, arranged in a regular topology to approximate a freeform surface, can form stable assemblies. Consider the two cubes of Figure 2-a. Assuming no friction forces act on the interface, a necessary condition for the cubes to form a stable stack is that the contact plane is orthogonal to the direction of gravity. In addition, we require that the center of gravity of the top block projects down into the contact polygon. This arrangement is in static equilibrium, but this equilibrium itself is not stable. Even the slightest tilt of the stack in any direction will cause the top block to slide and topple off.

Now let us consider three blocks (Figure 2-b). The light gray block on top has two contacts, each constraining its motion in the

---

Authors' addresses: Ziqi Wang, EPFL, ziqi.wang@epfl.ch; Peng Song, EPFL, Singapore University of Technology and Design, peng_song@sutd.edu.sg; Florin Isvoranu, EPFL, florin.isvoranu@epfl.ch; Mark Pauly, EPFL, mark.pauly@epfl.ch.

0730-0301/2019/11-ART193 $15.00
https://doi.org/10.1145/3355089.3356489

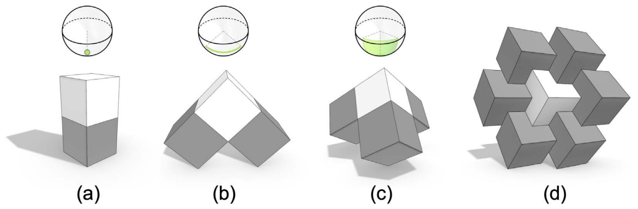

Fig. 2. Stability of cubes. Assuming the dark gray cubes are fixed and no friction forces act on the contact surfaces, the light gray cube is supported for a single gravity direction (a), an arc of directions (b), a patch of directions (c), and all directions (d).

direction orthogonal to the contact plane. In this case, we can tilt the ensemble around the axis defined by the intersection of the contact planes and retain an equilibrium state. Effectively, the space of tilt directions under which the assembly is in equilibrium has been expanded from a single point to a 1D arc.

Adding a third support block allows creating a 2D set of equilibrium directions (Figure 2-c). The top block is now in a stable configuration when tilting the ground plane around an arbitrary axis in some limited angle range. For a single cube to be completely immobilized no matter how the ensemble is rotated, we would need to constrain all six contact planes (Figure 2-d). In fact, this arrangement can be extended to form a regular assembly of cubes that cover the plane (see Figure 5-b). This specific pattern forms a so-called *topological interlocking* (TI) assembly [Dyskin et al. 2019]. Assuming the boundary is fixed, all interior cubes are mutually blocking each other. More specifically, this arrangement also forms a *globally interlocking* structure, where each part and each subset of parts is immobilized [Song et al. 2012].

Do we always need six neighbors to completely immobilize a convex element? The answer is no, because we can construct a non-empty polytope by intersecting four planes, hence a block constructed in this way can be completely immobilized by four neighbors. This construction is well known and has been used, for example, in the Abeille vault structure shown in Figure 3. These types of planar regular assemblies composed of identical blocks have been extensively studied in material science and mechanical engineering, where they have proven to have superior structural properties; see detailed discussion in Section 2.

So can we extend this concept from planar assemblies to curved freeform surfaces? And can we retain the advantageous structural properties of planar TI assemblies, in particular the global interlocking property? It is clear that we cannot use identical elements if we want to closely approximate a double curved surface. However, we can easily modify the shapes of the blocks so that the assembly conforms well to a given design surface [Fallacara et al. 2019]. For example, the assembly shown in Figure 4, created by a constructive method detailed later, well approximates a spherical design surface. Each block in this assembly is immobilized by its neighbors, i.e., no block can move if we assume each adjacent block is fixed. With the global peripheral constraint given by a complete ring of fixed boundary blocks shown in dark gray, the assembly should then be globally interlocking.

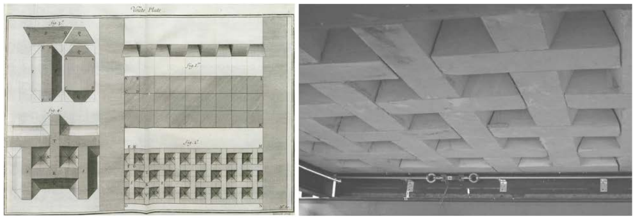

Fig. 3. The Abeille vault (sketch from 1734 on the left) is a globally interlocking assembly composed of identical convex blocks that form a planar roof structure (right).

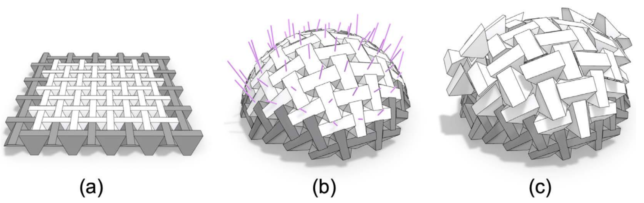

Fig. 4. A globally interlocking assembly following Abeille's construction (a) is lifted onto a spherical surface (b). While each block is still immobilized with respect to its neighbors, a subset of blocks can move simultaneously along different trajectories (c). The purple lines in (b) indicate the instantaneous velocity of each block for this disassembly motion. As a consequence, the assembly is *not* globally interlocking.

Unfortunately, this reasoning is flawed. While it is true that no block can move individually, sub-groups of blocks can move *simultaneously* along different trajectories (see also supplementary video). This kind of multi-part instability is not captured by existing methods and provides a first indication that globally interlocking TI assemblies are difficult to obtain for curved surfaces. Motivated by this observation, we focus on designing TI assemblies that are as close to global interlocking as possible.

Contributions. Our goal is to design structurally stable assemblies with convex rigid blocks that closely conform to a given design surface. We focus in this paper on convex elements with planar faces because they can easily be fabricated by blade or wire cutting, but also because of their superior structural integrity [Alexandrov 2005]. Geometrically, however, the convexity of blocks poses the biggest challenge in terms of creating stable assemblies, because two adjacent parts are only constrained in one direction by their mutual contact. To address this challenge, we make the following contributions:

- We introduce a new, general algorithm to test for global interlocking that considers not only part translation, but also rotation, thus avoiding false positives that can occur with existing methods.
- We formalize a theoretical link between static equilibrium conditions and a global interlocking property with a mathematical proof.
- We propose a quantitative measure for structural stability of assemblies and present a gradient-based method that optimizes the geometry of blocks to maximize this measure.

- We develop an interactive design tool that allows a real-time preview and efficient exploration of a wide range of design parameters of TI assemblies.

Overview. The rest of the paper is organized as follows: We first discuss related work in Section 2. Section 3 reviews the mathematical formulation of static equilibrium analysis and our global interlocking test, and establishes a formal connection between them. Section 4 introduces a stability measure that can be interpreted as a structural condition in-between single-load equilibrium and global interlocking. Section 5 introduces a parametric model for TI assemblies that facilitates a constructive approach for design exploration. Section 6 presents a gradient-based optimization to improve the structural stability of an assembly with respect to the measure. In Section 7 we show and discuss a variety of TI assemblies designed by our approach. We conclude with a discussion of limitations of our approach and identify opportunities for future research.

2 RELATED WORK

Our research is situated at the interface of computer graphics, structural engineering, and architectural design, and we discuss the most related previous work in these fields below. Specifically, we focus on computational methods for interlocking assemblies, self-supporting structures, structural optimization, and TI assemblies.

Interlocking Assemblies. In an interlocking assembly, there is only one movable part, called the *key*, while all other parts as well as any subset of parts are immobilized relative to one another by their geometric arrangement [Song et al. 2012]. Starting from the key, the assembly can be gradually disassembled into individual parts by following specific orders.

Several computational methods have been developed to construct interlocking assemblies for different applications, including puzzles [Song et al. 2012; Tang et al. 2019; Xin et al. 2011], 3D printed objects [Song et al. 2015; Yao et al. 2017a], laser-cut polyhedrons [Song et al. 2016], and furniture [Fu et al. 2015; Song et al. 2017]. Zhang and Balkcom [2016] explored a small set of reusable voxel-like interlocking blocks for building 3D structures, while Wang et al. [2018] developed a unified framework to design interlocking assemblies of different forms by leveraging a graph-based representation.

The above works achieve the challenging goal of making an assembly interlocking by constructing parts with irregular shape or integral joints that closely constrain the relative inter-part motion. In contrast, our TI assemblies are composed of simple convex blocks and a boundary frame that holds the entire structure. This makes it difficult to obtain TI assemblies that are *globally* interlocking, since planar contacts between the convex blocks have relatively weak capability to restrict inter-block movement.

Self-supporting Structures. A self-supporting structure is an arrangement of blocks without external supports that is in static equilibrium with gravity-induced compression forces holding all the blocks in place. According to the safety theorem [Heyman 1966], a structure is self-supporting if there exists a thrust surface contained within the structure that forms a compressive membrane resisting the load applied to the structure. Several papers proposed computational design methods for freeform self-supporting surfaces [de Goes et al. 2013; Liu et al. 2013; Miki et al. 2015; Tang et al. 2014; Vouga et al. 2012]. From these, self-supporting structures can be generated by thickening the surface and partitioning it into multiple blocks [Panozzo et al. 2013; Rippmann et al. 2016].

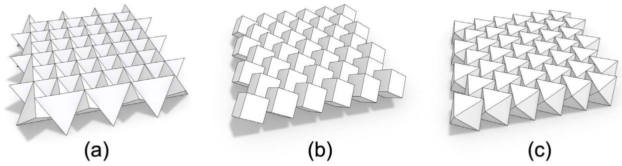

Fig. 5. Example planar TI assemblies described in [Dyskin et al. 2003a] composed of (a) tetrahedrons, (b) cubes, and (c) octahedrons.

Different from the continuous concept of self-supporting surfaces, the design of TI assemblies is discrete in nature, since the stability of the assembly directly relies on the blocks' geometry and their mutual arrangement, rather than on specific properties of the underlying design surface. As we show in this paper, TI assemblies can be in static equilibrium for a cone of directions and even become globally interlocking for certain geometries, without relying on friction between the blocks. They can also approximate surfaces that are not self-supporting; see Section 7.

Stability Analysis and Structural Optimization. The equilibrium method [Shin et al. 2016; Whiting et al. 2009; Yao et al. 2017b] is the current state of the art for stability analysis of 3D assemblies in graphics and architecture. This approach assumes rigid component parts and focuses on the balance of the external forces acting on each part. Whiting and colleagues [2009] integrated the equilibrium method with procedural modeling to design structurally sound masonry, and later extended the approach with a gradient descent optimization [Whiting et al. 2012]. The stability of masonry structures under lateral acceleration also can be analyzed based on static equilibrium [Ochsendorf 2002; Zessin 2012], which can be simulated with a tilt analysis that rotates the ground plane of the structure to apply both a horizontal and vertical acceleration to the structure; see the inset. For a given rotation axis, the critical tilt angle ϕ gives the minimum value of lateral acceleration to cause the structure to collapse, providing a measure of the structure's lateral stability [Shin et al. 2016; Yao et al. 2017b]. We generalize this measure by considering all possible azimuthal tilt directions and develop a structural optimization method that improves the stability of TI assemblies with respect to this measure by varying the the blocks' geometry.

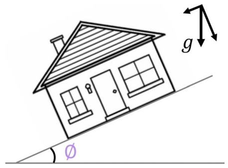

Topological Interlocking Assemblies. The principle of TI assemblies was discovered during the Renaissance when French architect Joseph Abeille realized a flat vault with truncated tetrahedrons that can support itself [Brocato and Mondardini 2012; Vella and Kotnik 2016]. In 1984, the same principle was used by Glickman [1984] for developing a new paving system. It was later found that a planar TI assembly can be constructed from all platonic bodies [Dyskin et al. 2003a]; see Figure 5 for some examples.

Several other works in material science study the design of new TI blocks for planar structures. Dyskin et al. [2013] proposed a method to construct the shape of convex TI elements from a tiling of the middle plane. Weizmann et al. [2016; 2017] explored different 2D tessellations (regular, semi-regular and non-regular tessellations) to discover new TI blocks for building floors. Besides convex polyhedra, elements with curved contact surfaces can also form planar TI assemblies [Dyskin et al. 2003b; Javan et al. 2016]; please refer to [Dyskin et al. 2019] for a thorough overview. Physical experiments conducted on these TI assemblies show that they possess interesting and unusual mechanical properties, including high strength and toughness [Mirkhalaf et al. 2018], damage confinement [Siegmund et al. 2016], and avoiding failure under high amplitude vibrations [Schaare et al. 2009].

Motivated by the intriguing properties of planar TI assemblies, researchers in architecture studied the design of freeform 3D TI assemblies [Fallacara et al. 2019]. Tessmann [2012] presented a catalogue of parametric elements that can form an architectural TI structure. Weizmann et al. [2016] designed TI assemblies with curvilinear shape by projecting a 2D tessellation onto a curved surface and constructing the TI blocks following the surface curvature. Bejarano and Hoffmann [2019] proposed a constructive approach to generate 3D TI assemblies that maintain alignment of the blocks, focusing purely on the geometric design without considering fabrication and assembly. Although several experimental prototypes have been shown in some of the above works, no analysis or optimization of the structural behavior is given, nor is the concept of global interlocking systematically studied.

Our work quantifies, for the first time, the structural stability of TI assemblies from a geometric perspective, formulates the design of structurally stable freeform TI assemblies as a geometric optimization over a parametric model of the assembly, and presents an interactive tool that allows users to control various design parameters and to optimize the assembly for improving the stability.

3 ASSEMBLY STABILITY ANALYSIS

We study TI assemblies with convex rigid blocks that can exhibit two types of contacts, face-face and edge-edge contacts as illustrated in Figure 6. We represent a TI assembly with n component parts as $\mathbf{P} = \{P_i\}$, where P_i $(1 \leq i < n)$ is a block and P_n is the boundary frame that defines the global peripheral constraint. In this section, we first present the mathematical formulation for identifying two structurally stable states of TI assemblies, *global interlocking* and *static equilibrium*, and then make a formal connection between these two states with a mathematical proof.

3.1 Global Interlocking Test

To test global interlocking of a given 3D assembly, we need to test immobilization (or mobility) of each part and each part group. Existing works assume that translational motions are sufficient for disassembly, and that rotational part motions are generally not required. These methods focus on 3D assemblies with orthogonal parts connection [Song et al. 2012; Xin et al. 2011] or with integral joints that only allow translational motion of parts [Fu et al. 2015; Wang et al. 2018; Yao et al. 2017a]. As a consequence, parts or part groups that are movable along a finite number of translational directions can be identified either with exhaustive search [Song et al. 2012] or a more efficient graph-based approach [Wang et al. 2018].

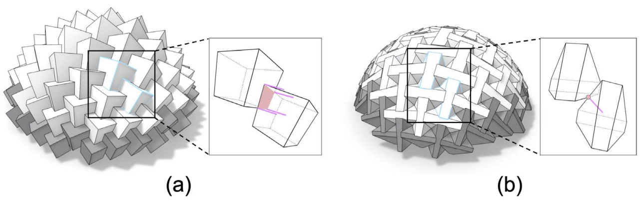

Fig. 6. Two types of contacts in TI assemblies: (a) face-face and (b) edge-edge contacts. The contact region between the two blocks (with cyan frame) is colored in red while the discretized interaction force at each contact vertex is shown as a purple vector.

In our TI assemblies, however, adjacent blocks have only a single planar contact (i.e., no complex joint); see Figure 6. In such assemblies, it is possible that parts (or part groups) can be taken out from the assembly with rotation(s) but not translation(s); see the inset for an example, which is reproduced from [Wilson and Matsui 1992]. It is therefore essential to consider both translation and rotation of each individual part and each part group when testing for global interlocking, which renders existing approaches inapplicable. To address this challenge, we propose a general algorithm to test global interlocking based on solving the well-known non-penetration linear inequalities in a rigid body system [Kaufman et al. 2008].

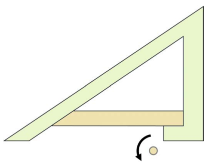

For a TI assembly $\mathbf{P}$ with n component parts and m contacts, we denote the polygonal contact between P_i and P_j as C_l $(l \in [1, m])$, vertices of C_l as $\{c_k\}$ where $1 \leq k \leq v_l$ $(v_l = |\{c_k\}|)$, and normal of C_l as $\mathbf{n}_l$. We enforce that $\mathbf{n}_l$ always points towards the part with the larger index. To simplify notation, we assume $i < j$ and thus $\mathbf{n}_l$ always points towards P_j; see Figure 7-a.

We model both types of contacts in TI assemblies (see Figure 6) as a set of point-plane contact constraints:

- A *face-face contact* constraint is modeled as a set of point-plane constraints at the vertices of the (convex) contact polygon; see Figure 6-a.
- An *edge-edge contact* constraint is modeled as a point-plane constraint between the contact point and the plane containing the two edges, whose normal is denoted as $\mathbf{n}_l$ also; see Figure 6-b.

Consider that each rigid part P_i can translate and rotate freely in 3D space. We denote the linear velocity of P_i as $\mathbf{t}_i$, the angular velocity of P_i as $\boldsymbol{\omega}_i$, and the local motion of P_i as a 6D spatial vector $\mathbf{Y}_i = [\mathbf{t}_i^T, \boldsymbol{\omega}_i^T]^T$; see Figure 7-a. For an arbitrary vertex c_k (abbreviated as c in the following equations) on the contact C_l between P_i and P_j, $\mathbf{Y}_i$ and $\mathbf{Y}_j$ will cause c to undergo an infinitesimal motion together with P_i and P_j respectively:

$$\mathbf{v}_i^c = \mathbf{t}_i + \boldsymbol{\omega}_i \times \mathbf{r}_i^c \tag{1}$$

$$\mathbf{v}_j^c = \mathbf{t}_j + \boldsymbol{\omega}_j \times \mathbf{r}_j^c \tag{2}$$

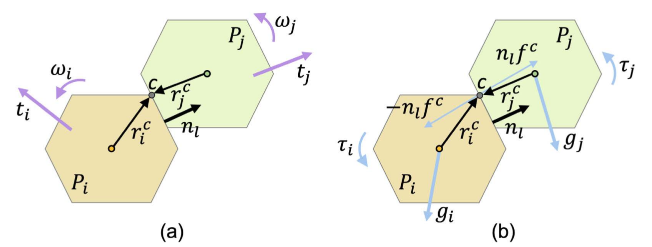

(a) (b)

Fig. 7. Two parts P_i and P_j have a planar contact, where c is a point on the contact interface and $\mathbf{r}_i^c$ is a vector from P_i's centroid to c (analogously for $\mathbf{r}_j^c$). (a) P_i and P_j should not collide with each other at the contact during their movement, e.g., translation $\mathbf{t}_i$ and rotation $\boldsymbol{\omega}_i$ of P_i. (b) Each block P_i is in equilibrium if there exists a system of interaction forces (e.g., $-\mathbf{n}_l f^c$) that balance the external force $\mathbf{g}_i$ and torque $\boldsymbol{\tau}_i$ acting on it.

During the parts movement, the constraint is to avoid collision at their contacts. Since our interlocking test considers only infinitesimal motions of each block, we assume that the contact points remain fixed during the test. Hence, the collision-free constraint between P_i and P_j at contact point c can be modeled as:

$$(\mathbf{v}_j^c - \mathbf{v}_i^c) \cdot \mathbf{n}_l \geq 0 \tag{3}$$

By substituting Equations 1&2 in Equation 3, we obtain:

$$\begin{bmatrix} -\mathbf{n}_l^T & -(\mathbf{r}_i^c \times \mathbf{n}_l)^T & \mathbf{n}_l^T & (\mathbf{r}_j^c \times \mathbf{n}_l)^T \end{bmatrix} \begin{bmatrix} \mathbf{Y}_i \\ \mathbf{Y}_j \end{bmatrix} \geq \mathbf{0} \tag{4}$$

Equation 4 describes the constraint of a point-plane contact between P_i and P_j. By stacking the point-plane constraint in Equation 4 for each vertex of each contact in the TI assembly $\mathbf{P}$, we obtain a system of linear inequalities:

$$\mathbf{B}_{\text{in}} \cdot \mathbf{Y} \geq \mathbf{0} \qquad \text{s.t.}\ \ \mathbf{Y} \neq \mathbf{0} \tag{5}$$

where $\mathbf{Y}$ is the generalized velocity of the rigid body system $\{P_i\}$, and $\mathbf{B}_{\text{in}}$ is the matrix of coefficients for the non-penetration constraints among the blocks in the system (see the supplementary material).

To avoid the case that the assembly moves as a whole, we fix an arbitrary part, usually the boundary frame P_n, by setting $\mathbf{Y}_n = \mathbf{0}$. We consider the assembly $\mathbf{P}$ as globally interlocking, if the system in Equation 5 does not have any non-zero solution.[1] We solve the system by formulating a linear program following [Wang et al. 2018]; please refer to the supplementary material for details.

Our formulation of the global interlocking test allows for a very efficient implementation. For example, it took 0.98 seconds to perform the test on the assembly of Figure 1 composed of 62 parts. More importantly, our interlocking test is more general than previous methods [Song et al. 2012; Wang et al. 2018]. It can test for global interlocking of arbitrary 3D assemblies with rigid parts where the part contacts can be modeled as a set of point-plane contact constraints [Wilson and Matsui 1992], no matter whether the parts are orthogonally or non-orthogonally connected, or what kinds of joints are used to connect the parts.

3.2 Static Equilibrium Analysis

Lets us now consider how to analyze an assembly for static equilibrium. Let $\mathbf{g}_i$ be the external force and $\boldsymbol{\tau}_i$ the torque acting on part P_i of an assembly $\mathbf{P}$; see Figure 7-b. Let $\mathbf{W}_i = [\mathbf{g}_i^T, \boldsymbol{\tau}_i^T]^T$. Given all the external forces and torques $\mathbf{W} = [\mathbf{W}_1^T, \ldots, \mathbf{W}_n^T]^T$, static equilibrium analysis computes the interaction forces between the parts and determines whether there exists a network of interaction forces that lead to a static equilibrium state.

We perform the equilibrium analysis following the method in [Whiting et al. 2009] with two main modifications to make it suitable for TI assemblies:

- We ignore friction among the parts to avoid any dependence on physical material properties. Friction forces can be unreliable in practice, e.g., due to fabrication inaccuracies or material wear. As a consequence, our analysis is more conservative and only relies on the geometry of assembly parts.
- Blocks in TI assemblies have two types of contacts, i.e., face-face and edge-edge contacts rather than face-face contacts only [Whiting et al. 2009]; see Figure 6.

To discretize contact forces, we assign a 3D force to each vertex of each contact, and assume a linear force distribution across the contact polygon (for the face-face contacts only); see again Figure 6. Since we ignore friction, the compressive contact force is always perpendicular to the contact interface. For a vertex c in C_l between P_i and P_j ($i < j$), we denote the contact force size as f_l^c ($f_l^c \geq 0$). Hence, the contact force applied on P_i is $-\mathbf{n}_l\, f_l^c$, and consequently $\mathbf{n}_l\, f_l^c$ on P_j. Static equilibrium conditions require that the net force and the net torque for each block P_i are equal to zero:

$$\sum_{l \in L(i)} \sum_{k=1}^{v_l} -\mathbf{n}_l\, f_l^{c_k} \;=\; -\mathbf{g}_i \tag{6}$$

$$\sum_{l \in L(i)} \sum_{k=1}^{v_l} -(\mathbf{r}_i^{c_k} \times \mathbf{n}_l)\, f_l^{c_k} \;=\; -\boldsymbol{\tau}_i \tag{7}$$

where $L(i)$ enumerates the contact IDs between P_i and its neighboring parts.

Combining the equilibrium constraints in Equation 6 and 7 for each block gives a linear system of equations:

$$\mathbf{A}_{\text{eq}} \cdot \mathbf{F} = -\mathbf{W} \qquad \text{s.t.}\ \ \mathbf{F} \geq \mathbf{0} \tag{8}$$

where $\mathbf{F}$ represents the unknown interaction forces in the assembly (i.e., contact force sizes at each vertex of each contact C_l), $\mathbf{A}_{\text{eq}}$ is the matrix of coefficients for the equilibrium equations [Whiting et al. 2009], and $\mathbf{W}$ represents the external forces and torques acting on the system, usually the weight of each part only without any torque. We solve Equation 8 following the approach in [Whiting et al. 2009]. In our implementation, it took 0.22 seconds to perform equilibrium analysis (under gravity) for the TI assembly in Figure 1.

3.3 Connection between Interlocking and Equilibrium

Interlocking and equilibrium describe two specific structural states of 3D assemblies. We make a formal connection between interlocking and equilibrium as follows:

---

[1] To make the TI structure disassemblable, we will eventually break the boundary frame into two subparts, among which one subpart will form the key that will be taken out from the structure first.

> An *interlocking* assembly is an assembly that is in *equilibrium* under arbitrary external forces and torques.

This connection relies on the fact that the coefficient matrix $\mathbf{B}_{\text{in}}$ in Equation 5 and $\mathbf{A}_{\text{eq}}$ in Equation 8 are transposed to each other, according to the well-known close relation between velocity kinematics and statics [Davidson and Hunt 2004].

The above statement can be formally proved based on a solvability theorem for a finite system of linear inequalities, in particular Farkas' lemma [Farkas 1902]:

LEMMA 3.1 (FARKAS' LEMMA). *Let* $\mathbf{A} \in \mathbb{R}^{n \times m}$ *and* $\mathbf{b} \in \mathbb{R}^n$. *Then the following two statements are equivalent:*

(1) There exists an $\mathbf{x} \in \mathbb{R}^m$ *such that* $\mathbf{A}\mathbf{x} = \mathbf{b}$ *and* $\mathbf{x} \geq \mathbf{0}$.
(2) There does not exist a $\mathbf{y} \in \mathbb{R}^n$ *such that* $\mathbf{A}^T\mathbf{y} \geq \mathbf{0}$ *and* $\mathbf{b}^T\mathbf{y} < \mathbf{0}$.

Our observation is that the mathematical formulations of equilibrium and interlocking in Subsection 3.2 and 3.1 correspond to the first and second statement in Farkas' lemma, respectively. In particular, $\mathbf{A} = \mathbf{A}_{\text{eq}}$, $\mathbf{x} = \mathbf{F}$, and $\mathbf{b} = -\mathbf{W}$ relate statement 1 to Equation 8 while $\mathbf{A}^T = \mathbf{B}_{\text{in}}$ and $\mathbf{y} = \mathbf{Y}$ relate statement 2 to Equation 5.

By assuming that $\mathbf{b} = -\mathbf{W}$ can be an arbitrary vector (i.e., arbitrary external forces and torques), we can see that the condition of $\mathbf{b}^T\mathbf{y} < 0$ in statement 2 is equivalent to $\mathbf{y} \neq \mathbf{0}$. Statement 2 then becomes exactly consistent with the formulation of interlocking in Equation 5 and the formal connection between interlocking and equilibrium is proved.

Discussion. Our assembly stability analysis is related to structural rigidity theory [Thorpe and Duxbury 2002], whose typical application is to design tensegrity structures [Pietroni et al. 2017]. In this theory, structures are formed by collections of rigid components such as straight rods, with pairs of components connected by flexible linkages such as cables (in contrast, our parts are connected purely by their planar contacts). A structure is rigid if there is no continuous motion of the structure that preserves the shape of its rigid components and the pattern of their connections at the linkages. Similar to the link that we made between interlocking and equilibrium, there are two equivalent concepts of rigidity: 1) infinitesimal rigidity in terms of infinitesimal displacements; and 2) static rigidity in terms of forces applied on the structure.

4 ASSEMBLY STABILITY MEASURE

Our analysis shows that static equilibrium means that the assembly is stable under a constant external force and torque configuration $\mathbf{W}$, while global interlocking indicates that the structure is stable under an arbitrary $\mathbf{W}$. In practice, ensuring static equilibrium for a single $\mathbf{W}$ might be insufficient since the assembly could be exposed to different forces (e.g., live loads). On the other hand, a global interlocking requirement might impose too strict constraints on the assembly's geometry, as real assemblies usually do not have to experience arbitrary external forces.

This motivates us to consider stability conditions that are more strict than single-load equilibrium, but not as restrictive as global interlocking; see Figure 8. Our idea for quantifying these stability conditions is based on the set of external force and torque configurations $\mathbf{W} \in \mathbb{R}^{6n}$ under which the assembly $\mathbf{P}$ is in equilibrium, denoted as the feasible set $\mathbb{G}(\mathbf{P})$, which has the following properties:

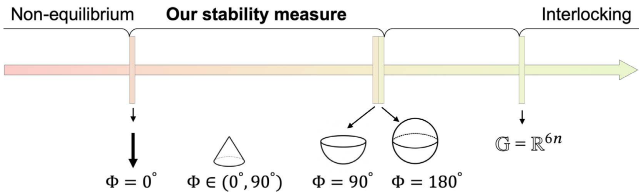

Fig. 8. Spectrum of assembly stability in which the stability increases from left to right, i.e., *non-equilibrium* (under single load, e.g., gravity), *equilibrium but not interlocking* that can be quantified by our stability measure Φ, and *global interlocking*. The gap between our stability measure and interlocking in the spectrum represents stability conditions where an assembly is in equilibrium under all possible gravity directions but not an arbitrary $\mathbf{W}$.

(i) If $\mathbf{W} \in \mathbb{G}$, then $\lambda\mathbf{W} \in \mathbb{G}$ $(\lambda \geq 0)$, since we can multiply both sides of Equation 8 with λ.
(ii) If $\mathbf{W}_1 \in \mathbb{G}$ and $\mathbf{W}_2 \in \mathbb{G}$, then $\lambda\mathbf{W}_1 + (1-\lambda)\mathbf{W}_2 \in \mathbb{G}$ $(\lambda \geq 0)$ due to the linearity of Equation 8.

Hence, $\mathbb{G}(\mathbf{P})$ forms a convex cone in $\mathbb{R}^{6n}$. The case where $\mathbb{G}(\mathbf{P}) = \mathbb{R}^{6n}$ indicates that the assembly is global interlocking.

Similar to [Whiting et al. 2009], we consider a specific class of external force and torque configurations for the analysis and design of TI assemblies, in which each part P_i experiences a force $\mathbf{g}_i$ that passes through P_i's center of mass (i.e., $\boldsymbol{\tau}_i = \mathbf{0}$) and has a constant size (i.e., $\|\mathbf{g}_i\|$ equals to P_i's weight). Moreover, we assume that all $\mathbf{g}_i$ have the same direction, denoted by the unit vector $\mathbf{d}$. This assumption is motivated by the tilt analysis for measuring lateral stability of masonry structures in architecture [Ochsendorf 2002; Zessin 2012]; see again the inset in Section 2. By this, we reduce the degrees of freedom of $\mathbf{W}$ from 6n to 2 (i.e., a normalized vector $\mathbf{d}$).

We represent each normalized force direction $\mathbf{d}$ in spherical coordinates as $\mathbf{d}(\theta, \phi)$, where $\theta \in [0^\circ, 360^\circ)$ is the azimuthal angle and $\phi \in [0^\circ, 180^\circ]$ is the polar angle (relative to $-z$, the gravity direction). To compute $\mathbb{G}(\mathbf{P})$ we need to find all $\mathbf{d}(\theta, \phi) \in \mathbb{G}(\mathbf{P})$. Here, we check if $\mathbf{d}(\theta, \phi) \in \mathbb{G}(\mathbf{P})$ by testing whether the assembly $\mathbf{P}$ is in equilibrium under external forces with direction $\mathbf{d}(\theta, \phi)$ by solving Equation 8. Assuming that an assembly $\mathbf{P}$ is in equilibrium under gravity (i.e.,

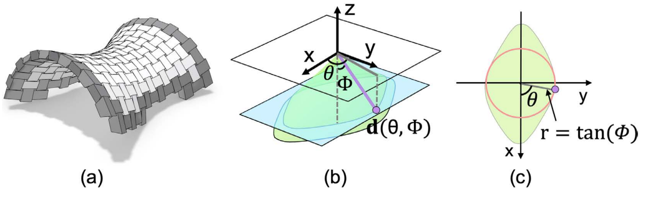

Fig. 9. (a) A TI assembly $\mathbf{P}$ and (b) its feasible cone $\mathbb{G}(\mathbf{P})$. (c) We visualize $\mathbb{G}(\mathbf{P})$ as the feasible section $\mathbb{S}(\mathbf{P})$ by intersecting it with the cyan plane ($z = -1$) in (b). The external force direction corresponding to our stability measure Φ is shown as a purple vector in (b) and a purple dot in (c). Note that the purple dot is the point of tangency between the feasible section $\mathbb{S}(\mathbf{P})$ and its largest inner circle (in red) centered at the origin.

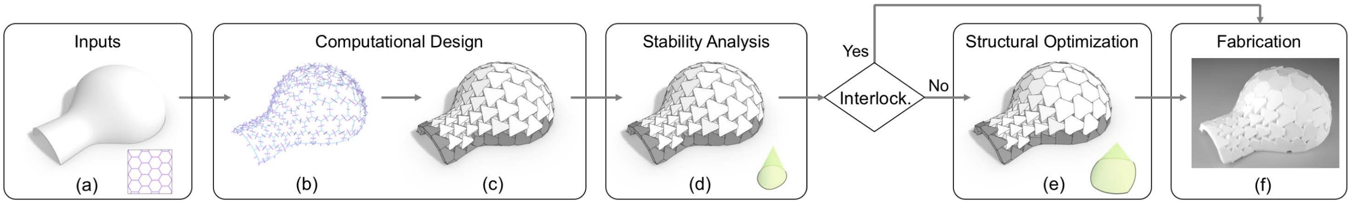

Fig. 10. Overview of our approach. (a) Input reference surface and 2D tessellation. (b) 3D surface tessellation with augmented vectors. (c) Initial TI assembly. (d) Stability analysis computes the cone of stable directions. (e) Structural optimization improves stability; i.e., the cone becomes larger. (f) 3D printed prototype.

$\mathbf{d}_g = (0, 0, -1) \in \mathbb{G}(\mathbf{P})$), we approximate $\mathbb{G}(\mathbf{P})$ by uniformly sampling θ and finding the critical ϕ for each sampled θ using binary search, thanks to the convexity of $\mathbb{G}$. Figure 9 shows an example feasible cone $\mathbb{G}(\mathbf{P})$ computed using our approach, as well as its cross section with plane $z = -1$, called the feasible section $\mathbb{S}(\mathbf{P})$.

Given the feasible cone $\mathbb{G}(\mathbf{P})$, we define our stability measure as:

$$\Phi(\mathbf{P}) \;=\; \min\{\; \phi \mid \mathbf{d}(\theta, \phi) \in \partial\mathbb{G}(\mathbf{P}) \;\} \tag{9}$$

where $\partial\mathbb{G}(\mathbf{P})$ denotes boundary of the feasible cone $\mathbb{G}(\mathbf{P})$. Our measure is actually the minimum critical tilt angle among all possible azimuthal tilt axes, which can be considered as a generalization of the critical tilt angle for a fixed axis [Zessin 2012]; see Figure 9-b&c. Figure 8 shows how our stability measure is embedded in the whole stability spectrum, where $\Phi = 0^\circ, 90^\circ, 180^\circ$ highlight some special stability states. Specifically, the stability states corresponding to $\Phi = 90^\circ$ and $\Phi = 180^\circ$ are adjacent in the spectrum since the feasible cone $\mathbb{G}(\mathbf{P})$ cannot be in-between a half sphere and a whole sphere due to the property of convexity.

5 COMPUTATIONAL DESIGN OF TI ASSEMBLIES

Given a reference surface $\mathbf{S}$ as input, our goal is to design a structurally stable TI assembly $\mathbf{P}$ that closely conforms to $\mathbf{S}$. To make this problem tractable, we first define a parametric model that facilitates a constructive approach for design exploration of TI assemblies. We then show in Section 6 how to optimize for the structural stability of a designed assembly. Figure 10 gives a high-level overview of our computational design pipeline.

5.1 Parametric Model

Dyskin et al. [2013] proposed a parametric model for planar TI assemblies based on a 2D polygonal tessellation $\mathbf{T}$ in which the edges are augmented with normalized vectors. We extend this model to parameterize 3D free-form TI assemblies using a 3D surface tessellation $\mathbf{T}$ with augmented vectors.

Parameter space. Specifically, we represent $\mathbf{T}$ as a polygon mesh using a half-edge data structure, where each face is denoted as T_i and each pair of half-edges shared by T_i and T_j is denoted as e_{ij} on T_i and e_{ji} on T_j. The 3D directional vector defined by each half-edge e_{ij} is denoted as $\mathbf{e}_{ij}$ with $\|\mathbf{e}_{ij}\| = 1$. We assign to each T_i a normal vector $\mathbf{N}_i$ defined by the least-squares plane of the polygon's vertices. We further augment each half-edge e_{ij} with a 3D vector $\mathbf{n}_{ij}$ where $\|\mathbf{n}_{ij}\| = 1$ and $\mathbf{n}_{ij} \perp \mathbf{e}_{ij}$; see Figure 11-a. Each half-edge e_{ij} together with the augmented vector $\mathbf{n}_{ij}$ defines a 3D plane.

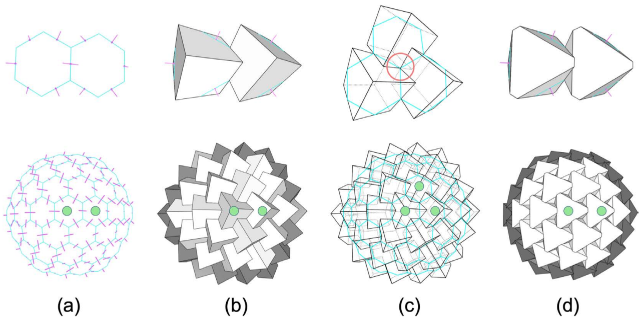

Fig. 11. A TI assembly is created from a 3D surface tessellation and a set of augmented vectors (a) by intersecting the half-spaces defined by each tessellation polygon (b). Each vertex of the tessellation corresponds to the joining point of neighboring blocks; see the red circle (c). Blocks can be additionally trimmed with surface offset planes (d). Zooming views of the faces/blocks highlighted with green dots are shown on the top row.

Block geometry. We intersect all 3D planes associated with the half-edges of each T_i to construct the (convex) geometry of the corresponding block P_i in $\mathbf{P}$; see Figure 11-b. Sometimes, the intersected block geometry could be infinite (or simply too bulky), so we optionally trim the blocks using offset planes with normal $\pm\mathbf{N}_i$; see Figure 11-d. Blocks corresponding to faces T_i in $\mathbf{T}$ that contain a boundary edge will be merged to form the boundary frame, shown in darker shading in the figures. The resulting boundary frame can also be clamped to a smooth outline; see for example Figure 15.

Valid assemblies. For the above construction method to produce a geometrically and structurally valid assembly, we restrict $\mathbf{T}$ to only contain convex faces that are not triangles as these would produce pyramid-shaped elements that cannot properly "interlock" with other blocks. We require $\mathbf{n}_{ij} = -\mathbf{n}_{ji}$ to ensure a proper planar contact face between adjacent blocks. We further require that each face T_i is in the half-space $(\mathbf{v} - \mathbf{v}_{ij}) \cdot \mathbf{n}_{ij} \le 0$ defined by each augmented half-edge of T_i, where $\mathbf{v}$ is an arbitrary point and $\mathbf{v}_{ij}$ is a point on the edge e_{ij}. This will ensure that the intersected geometry of P_i defined by the 3D planes $\{e_{ij}, \mathbf{n}_{ij}\}$ is not empty and encompasses the face T_i; see the zooming views in Figure 11-b&c.

5.2 Interactive Design

To initialize a design, the user selects a tessellation pattern, adapts global alignment and scaling, and assigns initial augmented vectors.

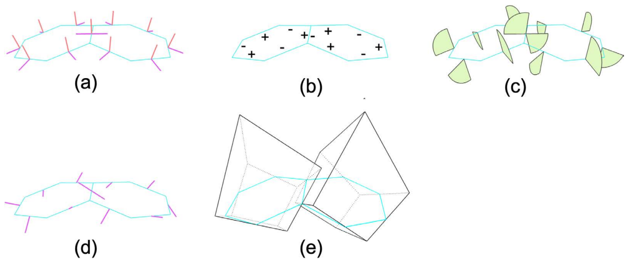

Fig. 12. (a) Initialize $\mathbf{n}_{ij}$ (in purple), where the red vector is $(\mathbf{N}_i + \mathbf{N}_j)/\|\mathbf{N}_i + \mathbf{N}_j\|$. (b) Determine orientations of $\mathbf{n}_{ij}$, where + (−) indicates clockwise (counterclockwise) rotation around $\mathbf{e}_{ij}$. (c) Compute range for each $\mathbf{n}_{ij}$ (visualized as green sectors). (d) Example $\{\mathbf{n}_{ij}\}$ generated with user-specified $\alpha = 35°$. (e) Two resulting blocks.

An automatic procedure that checks the above geometric requirements then provides immediate feedback on the assembly's validity. Specifically, our computational approach proceeds as follows:

Initialize tessellation. Given a reference surface **S**, there are many different ways to create a surface tessellation **T**, including remeshing, surface Voronoi diagrams, or parameterization approaches. Our tool mainly uses conformal maps to lift a planar tessellation onto the surface; see Figure 15 for examples. The user can interactively adjust the location, orientation, and scale of the tessellation. We further optimize the vertex positions using a projection-based optimization [Bouaziz et al. 2012; Deuss et al. 2015] to improve planarity and regularity of the 3D polygons and to ensure proper contacts among blocks by avoiding small dihedral angles. Please refer to the supplementary material for details about this optimization.

Assign vectors $\{\mathbf{n}_{ij}\}$. For each half-edge e_{ij} in the tessellation **T**, we initialize $\mathbf{n}_{ij}$ as $\mathbf{e}_{ij} \times (\mathbf{N}_i + \mathbf{N}_j)$ after normalization (see Figure 12-a). We then rotate $\mathbf{n}_{ij}$ around $\mathbf{e}_{ij}$ by an angle $x_{ij}\alpha_{ij}$, where each α_{ij} is initialized as a user-specified rotation angle α and $x_{ij} \in \{-1, 1\}$ specifies rotational direction (i.e., clockwise or counterclockwise). The goal here is to obtain alternating directions for adjacent edges of a polygon to improve the interlocking capabilities of blocks [Dyskin et al. 2019]. For this purpose, we use a simple flood-fill algorithm that starts with a random edge and traverses the half-edge data structure to assign $\{x_{ij}\}$ that locally maximize adjacent sign alternations. If all polygons have an even number of edges, this strategy can achieve global alternation (see Figure 12-b), which cannot be guaranteed in general, i.e., when the tessellation contains polygons with odd number of edges.

Select rotation angle α. The global parameter α can be interactively controlled by the user. For each edge we compute an allowable range $[\alpha_{ij}^{\min}, \alpha_{ij}^{\max}]$ that ensures a valid block geometry as defined above and clamp the applied rotation accordingly. Figure 13 shows 3D tessellations generated with different values of α. Due to the efficiency of this construction approach, the user can interactively create and preview TI assemblies while adjusting the design parameters, i.e. the 2D tessellation and its mapping onto the reference surface, the rotation angle α, and the thickness of the blocks. Please refer to the supplementary video for an interactive demo.

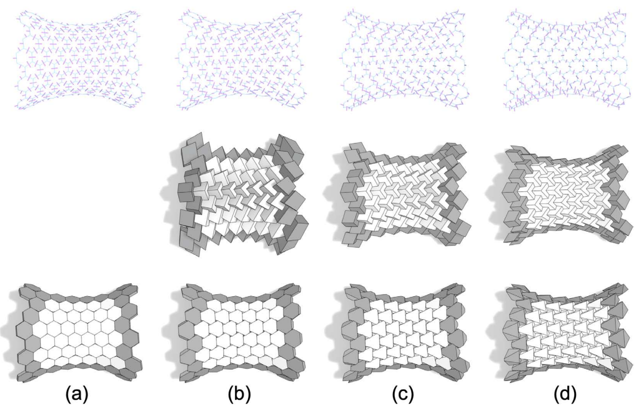

Fig. 13. TI assemblies generated with α equals to (a) 0°, (b) 25°, (c) 45°, and 65°. From top to bottom: 3D surface tessellation with augmented vectors, TI assemblies with originally constructed blocks, and with trimmed blocks. Note that the originally constructed blocks in the TI assembly with $\alpha = 0°$ have infinite geometry and thus are not shown.

6 STRUCTURAL OPTIMIZATION OF TI ASSEMBLIES

The interactive design stage generates a TI assembly **P** as input to the subsequent stages of our computational pipeline (Figure 10-d&e). If our analysis algorithm of Section 3.1 reveals that **P** is globally interlocking, no further optimization is required. Otherwise, we run a structural optimization that distinguishes several cases; see Algorithm 1. To make these computations tractable, we only optimize the augmented vectors $\{\mathbf{n}_{ij}\}$ while fixing the tessellation **T**.

In detail, if the initial design is not in static equilibrium under gravity, we first run an optimization to find a stable state (Section 6.2). If a stable configuration is found, we evaluate its stability score as discussed in Section 4. If $\Phi = 180°$, then no further optimization is required. If $\Phi = 90°$, then finding a static equilibrium for any force direction in the upper hemisphere without breaking equilibrium for the directions in the lower hemisphere will result in $\Phi = 180°$ due to convexity of the feasible set $\mathbb{G}(\mathbf{P})$. We therefore simply run our optimization for all the six axial directions. Finally, if $\Phi \in [0°, 90°)$, we optimize stability for an incrementally growing cone of directions (Section 6.1).

6.1 Compute Target Force Directions

Given a TI assembly **P** with stability measure $\Phi(\mathbf{P}) \in [0°, 90°)$, the radius of the largest inner circle (centered at the origin) of the feasible section $\mathbb{S}(\mathbf{P})$ is $\tan(\Phi)$; see again Figure 9(c). To improve the stability measure from Φ to $\Phi_{\text{tagt}} = \omega\Phi$ ($\omega > 1$), we need to modify the feasible section and enlarge the radius of its largest inner circle from $\tan(\Phi)$ to $\tan(\Phi_{\text{tagt}})$. To this end, we approximate the target feasible section $\mathbb{S}_{\text{tagt}}(\mathbf{P})$ with a convex polygon that completely contains the target circle with radius $\tan(\Phi_{\text{tagt}})$. The vertices $\{\mathbf{v}_k\}$, $1 \le k \le K$, of the polygon should be as close as possible to the current feasible section $\mathbb{S}(\mathbf{P})$ to require minimal change to the geometry of the

Algorithm 1 Algorithm of structural optimization on a TI assembly **P** to improve its stability.

```
function StructuralOptimization( $\mathbf{P}$ )
    $S \leftarrow$ StabilityAnalysis( $\mathbf{P}$ )                     ▷ See Section 3
    if $S$ = Interlocking then
        return
    else if $S$ = NonEquilibrium then
        if OptimizeAssembly( $\mathbf{P}$, $-z$ ) $\neq$ Success then
            return
    $\Phi \leftarrow$ ComputeStabilityMeasure( $\mathbf{P}$ )        ▷ See Section 4
    if $\Phi = 180^\circ$ then
        return
    else if $\Phi = 90^\circ$ then
        if OptimizeAssembly( $\mathbf{P}$, $\{\pm\mathbf{x}, \pm\mathbf{y}, \pm\mathbf{z}\}$ ) $\neq$ Success then
            return
    else
        $\omega \leftarrow \omega_c$                        ▷ $\omega_c = 1.2$ in our experiments
        while $\omega > \omega_t$ do                 ▷ $\omega_t = 1.01$ in our experiments
            $\Phi_{\text{tagt}} \leftarrow \omega\,\Phi$
            $\{\mathbf{d}_k\} \leftarrow$ ComputeTargetDirections( $\Phi_{\text{tagt}}$, $\mathbf{P}$ )
            if OptimizeAssembly( $\mathbf{P}$, $\{\mathbf{d}_k\}$ ) = Success then
                $\omega \leftarrow \omega_c$
                $\mathbf{P} \leftarrow \mathbf{P}^*$          ▷ $\mathbf{P}^*$ is the optimized assembly
            else
                $\omega \leftarrow \delta\,\omega$           ▷ $\delta = 0.95$ in our experiments
        return
```

blocks. In our experiments, we choose $K = 6$ as a trade-off between computation efficiency and approximation accuracy.

We initialize the vertices as a regular K-sided polygon that encloses the target circle and optimize their positions to minimize their distances to the current feasible section $\mathbb{S}(\mathbf{P})$; see supplementary material for details about the optimization. Figure 14-c shows an example target feasible section $\mathbb{S}_{\text{tagt}}(\mathbf{P})$ approximated with a hexagon using our approach, together with the current and target inner circles. Each vertex of the target feasible section (i.e., the hexagon) corresponds to a 3D force direction that is usually outside of the current feasible cone $\mathbb{G}(\mathbf{P})$; see the purple lines in Figure 14-d. We denote these target force directions corresponding to $\{\mathbf{v}_k\}$ as $\{\mathbf{d}_k\}$.

6.2 Optimize TI Assembly

Given the set of target force directions $\{\mathbf{d}_k\}$, the goal of our optimization is to include each direction $\mathbf{d}_k$ in the feasible cone $\mathbb{G}(\mathbf{P}^*)$ of the optimized assembly $\mathbf{P}^*$. If this optimization succeeds, we enlarge Φ_{tagt}, recompute the target force directions $\{\mathbf{d}_k\}$, and repeat the optimization. Otherwise, we have to lower the optimization goal by decreasing Φ_{tagt}, and repeat the optimization. Our optimization terminates when the stability measure Φ cannot be improved any more; see again Algorithm 1.

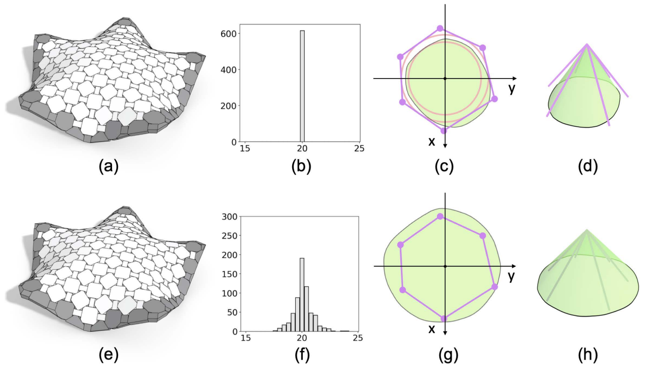

Fig. 14. An example TI assembly before (top) and after (bottom) one step of our optimization. (b&f) Histograms of vector rotation angles $\{\alpha_{ij}\}$, where each $\alpha_{ij} = \alpha$ (i.e., 20°) before the optimization. (c&d) Target force directions (in purple) in the feasible section and cone, where current and target circles are colored in red. (g&h) The optimization goal is achieved by including the target force directions in the optimized feasible section and cone.

Problem Formulation. Our optimization can be formulated as:

$$\{\alpha_{ij}^*\} = \underset{\{\alpha_{ij}\}}{\arg\min} \sum_{k=1}^{K} E(\ \mathbf{P},\ \mathbf{d}_k\ ) \tag{10}$$

$$\begin{aligned} \text{s.t.} \quad & \text{Area}(\ C_l\ ) \geq A_{\text{thres}}, \quad \forall \text{ contact } C_l \\ & \max(\alpha^{\min}, \alpha_{ij}^{\min}) \leq \alpha_{ij} \leq \min(\alpha^{\max}, \alpha_{ij}^{\max}) \end{aligned}$$

where $E(\mathbf{P}, \mathbf{d}_k)$ quantifies the assembly's infeasibility to be in equilibrium under external forces along direction $\mathbf{d}_k$; A_{thres} is the minimum allowable contact size among the blocks (for face-face contacts only); and $[\alpha^{\min}, \alpha^{\max}]$ is the user-specified range for every α_{ij} to preserve the assembly appearance while $[\alpha_{ij}^{\min}, \alpha_{ij}^{\max}]$ is the range for constructing blocks with valid geometry (see again Figure 12-c).

We compute the energy $E(\mathbf{P},\ \mathbf{d}_k)$ following the approach in [Whiting et al. 2012], where the key idea is to allow tension forces to act as "glue" at block interfaces to hold the assembly together, to penalize the tension forces, and to use their magnitude to quantify the infeasibility to be in static equilibrium.

In detail, we first express each contact force f_l^c at vertex c of contact C_l in terms of compression and tension forces using the difference of two non-negative variables:

$$f_l^c = f_l^{c+} - f_l^{c-} \qquad f_l^{c+},\ f_l^{c-} \geq 0 \tag{11}$$

where f_l^{c+} and f_l^{c-} are the positive and negative parts of f_l^c, representing the compression and tension forces, respectively. Our objective is to minimize tension forces between the blocks in the assembly $\mathbf{P}$ under external forces along direction $\mathbf{d}_k$, subject to the equilibrium constraint:

$$E(\ \mathbf{P},\ \mathbf{d}_k\ ) \ = \ \min_{\{\mathbf{f}_k\}} \mathbf{f}_k^T \mathbf{H} \mathbf{f}_k \tag{12}$$

$$\text{s.t.} \quad \mathbf{A}_{\text{eq}} \cdot \mathbf{F}_k = \mathbf{W}_k$$

where $\mathbf{f}_k$ is the vector of contact forces represented as $\{f_l^{c+}, f_l^{c-}\}$, $\mathbf{H}$ is a diagonal weighting matrix for the tension (large weights) and

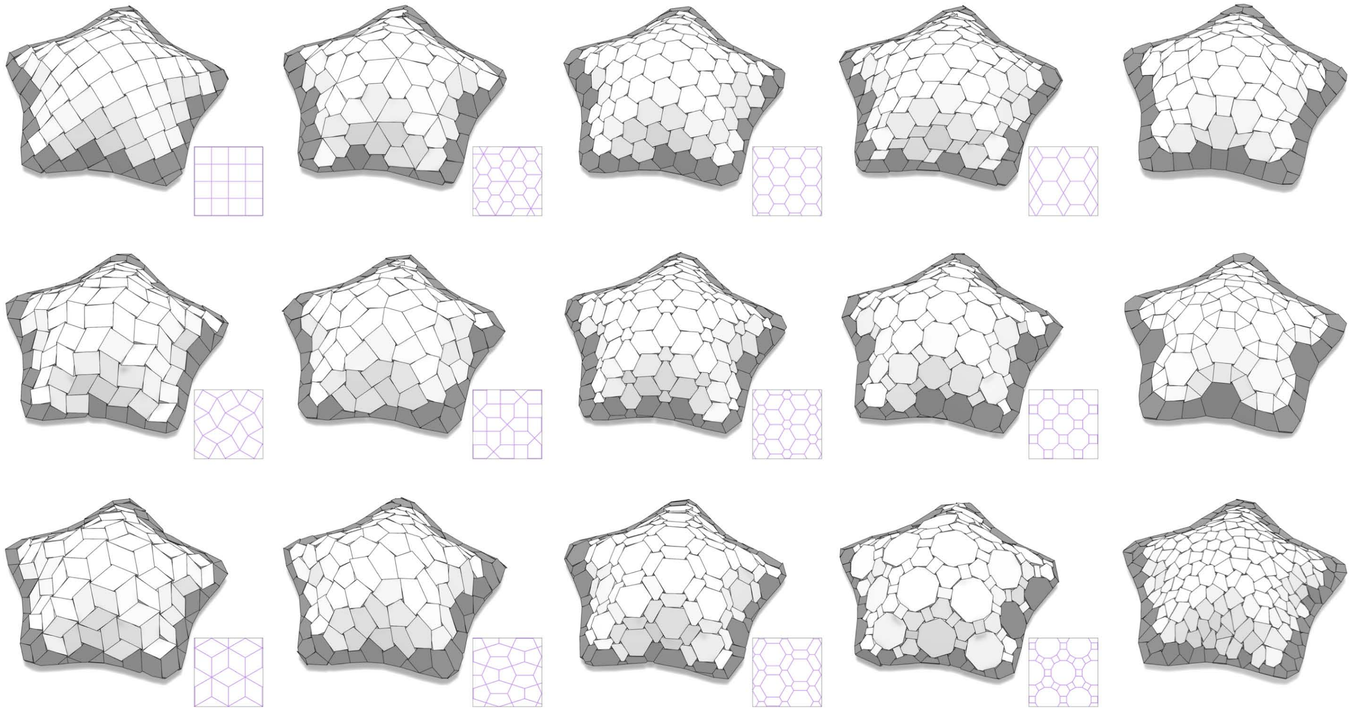

Fig. 15. A variety of patterns supported by our tool for designing TI assemblies. The surface tessellations can be generated by lifting 2D tessellations (see the boxed images) using conformal maps (the left four columns), manually designed by users (top two patterns in the rightmost column), or created as a surface Voronoi diagram (bottom pattern in the rightmost column).

compression (small weights) forces, $\mathbf{W}_k$ is the vector of external forces acting on each block along direction $\mathbf{d}_k$, and $\mathbf{F}_k$ is the vector of contact forces.

Optimization Solver. Our optimization in Equation 10 is very similar to the equilibrium optimization of 3D masonry structures [Whiting et al. 2012]. Hence, we solve our optimization following the gradient-based approach in [Whiting et al. 2012] with several important differences:

- Our optimization aims to achieve static equilibrium under forces along each target force direction in $\{\mathbf{d}_k\}$ respectively, rather than along a single gravitational direction.
- Our assemblies do not rely on friction, so we eliminate the friction constraints in the equilibrium condition in Equation 12.
- We compute the gradient of the energy $E(\mathbf{P}, \mathbf{d}_k)$ with respect to the vector rotation angles $\{\alpha_{ij}\}$, while [Whiting et al. 2012] computes it with respect to the positions of the block vertices; see the supplementary material for derivations of our gradients.

Figure 14 shows example TI assemblies before and after our optimization for a set of fixed target force directions $\{\mathbf{d}_k\}$. The histograms of the vector rotation angles $\{\alpha_{ij}\}$ show that our optimization adaptively adjusts these angles to make the assembly in static equilibrium for each of these force directions.

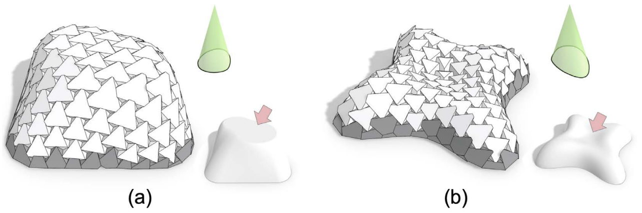

Fig. 16. Our method allows creating stable TI assemblies, indicated by the green feasible cones, even for design surfaces that are not self-supporting.

7 RESULTS AND DISCUSSION

We implemented our tool in C++ and OpenGL, and employed MOSEK [2019] and Knitro [2019] for solving our optimizations. We conducted all experiments on an iMac with a 4.2GHz CPU and 32GB memory. Our tool supports a variety of patterns as illustrated in Figure 15. We tested our design and optimization pipeline on a wide range of surfaces in Figure 17, e.g., FREE HOLES with high genus, FLOWER with zero mean curvature (i.e., minimal surface), and SURFACE VOUGA with both positive and negative Gaussian curvature. Figure 16 shows that our tool allows generating structurally stable TI assemblies from non-self-supporting surfaces, i.e. with a flat part or even an inverted bump on the top.

Table 1 summarizes the statistics of all the results presented in the paper. The third to sixth columns list the total number of parts,

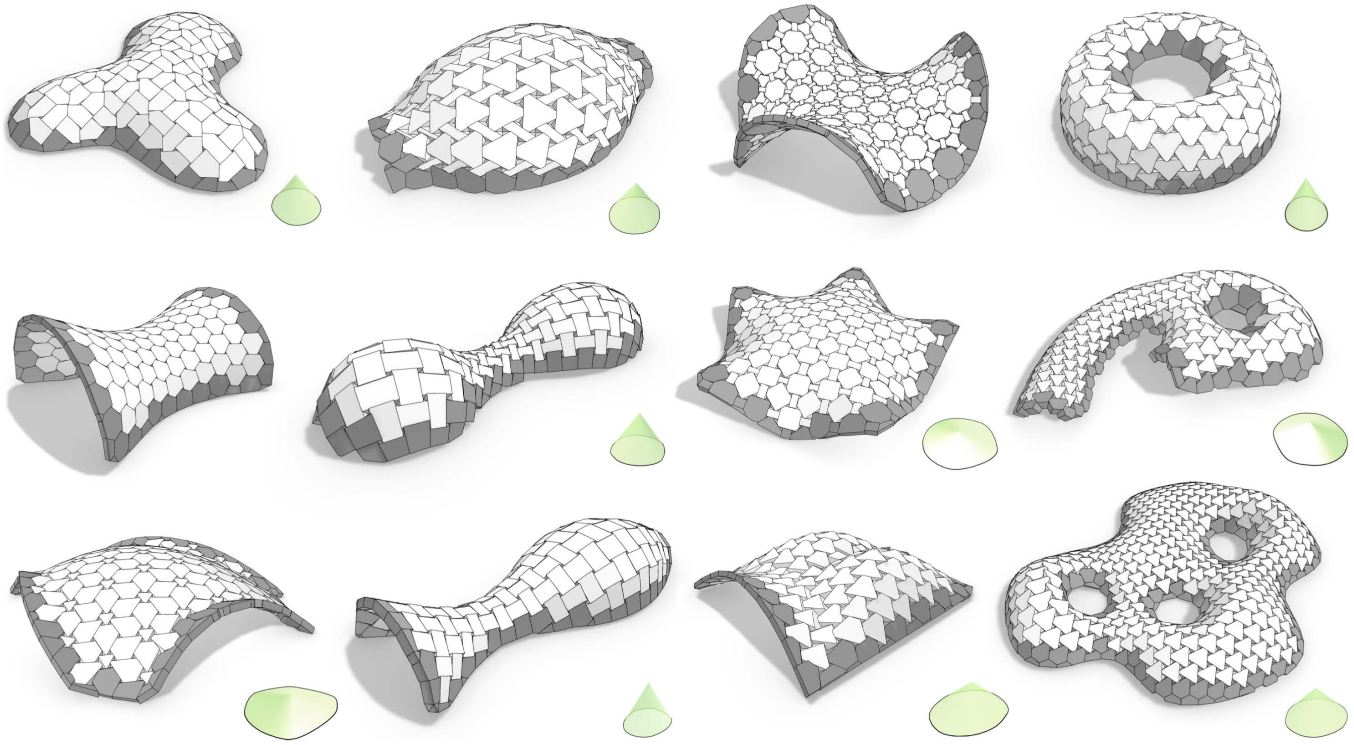

Fig. 17. TI assemblies of various shapes and their corresponding feasible cones (except those that are globally interlocking). From left to right and then top to bottom: Blob, Spindle, Flower, Torus, Hyperbolic, Peanut, Pentagon, Six, Buga Pavilion, Vase, Surface Vouga, and Free Holes.

Table 1. Statistics of the resulting TI assemblies in the paper.

Fig	Surface	# Part	# Contact	# Face-face contact	# Edge-edge contact	Before Optim. (degree)	After Optim. (degree)	Global Interlock	Init. Time (ms)	Optim. Time (min)
1	Roof	62	264	264	0	180.0	180.0	Yes	4.4	-
10	Igloo	64	274	274	0	22.2	29.4	No	4.7	30.7
16	Bump	110	408	408	0	0.8	13.4	No	2.3	474.4
	Lilium	105	432	432	0	-	16.2	No	5.6	259.8
17	Blob	113	522	381	141	-	31.7	No	5.1	798.7
	Spindle	133	589	426	163	1.4	31.8	No	6.3	78.1
	Flower	346	1192	1192	0	180.0	180.0	Yes	16.2	-
	Torus	120	507	507	0	10.6	25.7	No	6.7	54.5
	Hyperbolic	110	428	428	0	33.8	180.0	Yes	5.8	37.8
	Peanut	122	685	351	334	5.2	35.3	No	5.3	31.6
	Pentagon	190	740	740	0	31.9	78.5	No	12.7	471.1
	Six	138	580	580	0	33.1	65.0	No	7.7	1141.1
	Buga Pavilion	136	636	636	0	26.2	77.1	No	11.4	239.1
	Vase	95	565	291	274	14.6	36.5	No	4.7	24.1
	Surface Vouga	104	429	429	0	-	53.8	No	6.1	165.8
	Free Holes	345	1371	1371	0	18.3	46.6	No	17.4	340.0

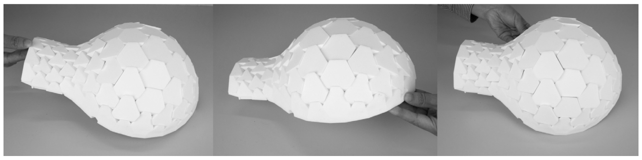

Fig. 18. Tilt analysis experiments on the 3D printed Igloo to validate its stability.

the total number of contacts, and the number of contacts for each specific type, respectively. As can be seen, face-face contacts are dominant in all the results. The seventh to ninth columns show the stability measure Φ before and after the optimization, and the interlocking test result on the assembly. In general, stability improves significantly; e.g., from non-equilibrium to $\Phi = 53.8^\circ$ for Surface Vouga, from $\Phi = 33.8^\circ$ to global interlocking for Hyperbolic. One interesting observation in our experiments is that TI assemblies constructed from a minimal surface are easy to be globally interlocking, even without structural optimization, e.g., Roof in Figure 1 and Flower in Figure 17. The tenth and eleventh columns show timing statistics of the TI geometry initialization from given parameters (in milliseconds) and the complete structural optimization on the geometry (in minutes), respectively.

Fabricated Prototypes. We fabricated two TI assemblies designed by our tool, Roof in Figure 1 and Igloo in Figure 10, using an SLS 3D printer with PA 2200 polyamide material. To ensure assemblability of the structure, we break the boundary frame into two separated components. We compute the assembly sequence based on disassembly. Starting from one boundary component as the key,

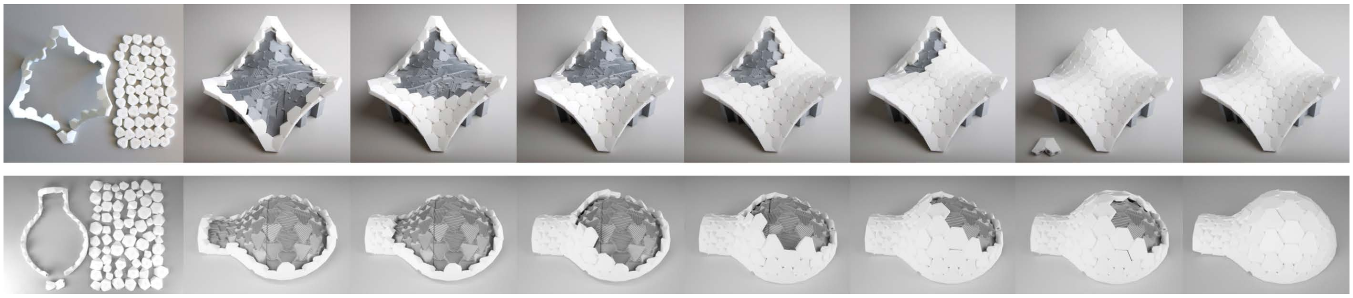

Fig. 19. Assembly sequence of (top) Roof and (bottom) Igloo, where the blocks and the boundary frame (in two components) are shown on the left. 3D printed formworks are used to support incomplete structures during the assembly.

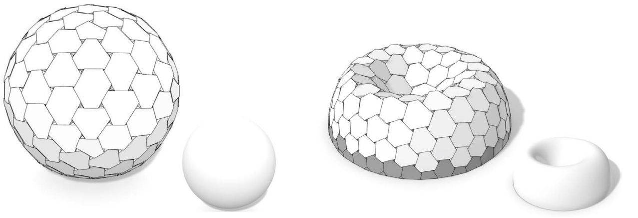

Fig. 20. Example shapes for which the optimization does not find an equilibrium under gravity.

we iteratively identify blocks that can be taken out from the structure, until the remaining boundary component. Figure 19 shows the assembly sequence of the two structures. Once all blocks are assembled, we close the boundary frame by adding the key boundary component, which is connected to its counterpart using integrated magnets. Figure 1 and 18 show physical experiments, including the tilt analysis, conducted on the two fabricated models, which validate their stability under different gravity directions. In particular, Roof in Figure 1 is stable under arbitrary orientations as predicted by its global interlocking property. Please watch the supplementary video for demos.

8 CONCLUSION

In this paper we studied how to approximate freeform design surfaces with structurally stable assemblies of convex rigid pieces. When analyzing their interlocking behavior, we observed that simultaneous multi-part motions and part rotations need to be considered when formulating a general algorithm to test for global interlocking. Our new formulation then led to the formalization of a link between the geometric property of global interlocking and force-based equilibrium conditions. This provided the key insight to formulate a general stability metric that is suitable for optimization. Our experiments show how this optimization allows creating structurally stable assemblies of convex elements that can approximate a wide variety of double-curved freeform surfaces.

However, not all input designs are suitable for our method. For certain models, for example, closed surfaces or surfaces with a significant concave cavity, our method does not find an equilibrium under gravity; see Figure 20 for two examples. In addition, we make a number of idealized assumptions. We model the boundary frame as a single part yet break the frame into two subparts for fabrication and assembly, which might affect prediction accuracy of our computational method. We also assume rigidity and perfect accuracy of the assembly blocks. For practical applications, questions related to fabrication tolerances and their effect on the global assembly are important, as accumulation of fabrication errors could lead to structural failure of a supposedly stable assembly.

Our stability measure considers load-induced external forces acting on the center of gravity of each block. As a consequence, our optimization only aims for static equilibrium under all possible gravity directions yet not under all possible force and torque configurations. This also means that we currently do not directly optimize for globally interlocking assemblies (see also Figure 8). Formulating a stability measure and corresponding optimization to support all possible force and torque configurations would be an interesting future work.

Our structural optimization adapts the rotation angles $\{\alpha_{ij}\}$ of the augmented vectors while keeping the surface tessellation fixed. Extending the method to also optimize the tessellation is an interesting research challenge. Another possible extension is to also consider non-convex blocks or curved contact surfaces. Other interesting future work is on finding optimal assembly sequences, e.g. with respect to the required support structure, improving the computational performance of the optimization, or analyzing and optimizing structural stability under element failure. Finally, interesting theoretical questions emerge. For example, what is the class of surfaces for which a globally interlocking assembly with convex blocks is possible? We expect minimal surfaces to be in this class, but we do not yet have a proof of this conjecture.

ACKNOWLEDGMENTS

We thank the reviewers for their valuable comments, Martin Kilian for providing surface models of Blob, Pentagon, and Free Holes, Daniele Panozzo for providing the Surface Vouga model, and Julian Panetta, Mina Konaković-Luković for proofreading the paper. This work was supported by the Swiss National Science Foundation (NCCR Digital Fabrication Agreement #51NF40-141853) and the SUTD Start-up Research Grant (Award Number: SRG ISTD 2019 148).

REFERENCES

A. D. Alexandrov. 2005. *Convex Polyhedra.* Springer.

MOSEK ApS. 2019. MOSEK software package. (2019). https://www.mosek.com/.

Artelys. 2019. Knitro software package. (2019). https://www.artelys.com/solvers/knitro/.

Andres Bejarano and Christoph Hoffmann. 2019. A Generalized Framework for Designing Topological Interlocking Configurations. *International Journal of Architectural Computing* (2019). online article.

Sofien Bouaziz, Mario Deuss, Yuliy Schwartzburg, Thibaut Weise, and Mark Pauly. 2012. Shape-Up: Shaping Discrete Geometry with Projections. *Comp. Graph. Forum (SGP)* 31, 5 (2012), 1657–1667.

M. Brocato and L. Mondardini. 2012. A New Type of Stone Dome Based on Abeille's Bond. *International Journal of Solids and Structures* 49, 13 (2012).

Joseph K. Davidson and Kenneth H. Hunt. 2004. *Robots and Screw Theory: Applications of Kinematics and Statics to Robotics.* Oxford University Press.

Fernando de Goes, Pierre Alliez, Houman Owhadi, and Mathieu Desbrun. 2013. On the Equilibrium of Simplicial Masonry Structures. *ACM Trans. on Graph. (SIGGRAPH)* 32, 4 (2013). Article No. 93.

Mario Deuss, Anders Holden Deleuran, Sofien Bouaziz, Bailin Deng, Daniel Piker, and Mark Pauly. 2015. ShapeOp - A Robust and Extensible Geometric Modelling Paradigm. In *Design Modelling Symposium.* 505–515. https://www.shapeop.org/.

Arcady Dyskin, Elena Pasternak, and Yuri Estrin. 2013. Topological Interlocking as a Design Principle for Hybrid Materials. In *Proceedings of the 8th Pacific Rim International Congress on Advanced Materials and Processing.* 1525–1534.

A. V. Dyskin, Y. Estrin, A. J. Kanel-Belov, and E. Pasternak. 2003a. Topological Interlocking of Platonic Solids: A Way to New Materials and Structures. *Philosophical Magazine Letters* 83, 3 (2003), 197–203.

A. V. Dyskin, Yuri Estrin, and E. Pasternak. 2019. Topological Interlocking Materials. In *Architectured Materials in Nature and Engineering*, Yuri Estrin, Yves Bréchet, John Dunlop, and Peter Fratzl (Eds.). Springer International Publishing, Chapter 2, 23—49.

A. V. Dyskin, Y. Estrin, E. Pasternak, H. C. Khor, and A. J. Kanel-Belov. 2003b. Fracture Resistant Structures Based on Topological Interlocking with Non-planar Contacts. *Advanced Engineering Materials* 5, 3 (2003), 116–119.

Giuseppe Fallacara, Maurizio Barberio, and Micaela Colella. 2019. Topological Interlocking Blocks for Architecture: From Flat to Curved Morphologies. In *Architectured Materials in Nature and Engineering*, Yuri Estrin, Yves Bréchet, John Dunlop, and Peter Fratzl (Eds.). Springer International Publishing, Chapter 14, 423—445.

Julius Farkas. 1902. Theorie der Einfachen Ungleichungen. *Journal für die Reine und Angewandte Mathematik* 124 (1902), 1 – 27.

Chi-Wing Fu, Peng Song, Xiaoqi Yan, Lee Wei Yang, Pradeep Kumar Jayaraman, and Daniel Cohen-Or. 2015. Computational Interlocking Furniture Assembly. *ACM Trans. on Graph. (SIGGRAPH)* 34, 4 (2015). Article No. 91.

Michael Glickman. 1984. The G-block System of Vertically Interlocking Paving. In *Proceedings of the 2nd International Conference on Concrete Block Paving.* 345–348.

Jacques Heyman. 1966. The Stone Skeleton. *International Journal of Solids and Structures* 2, 2 (1966), 249 – 279.

Anooshe Rezaee Javan, Hamed Seifi, Shanqing Xu, and Yi Min Xie. 2016. Design of A New Type of Interlocking Brick and Evaluation of Its Dynamic Performance. In *Proceedings of the International Association for Shell and Spatial Structures Annual Symposium.* 1–8.

Danny M. Kaufman, Shinjiro Sueda, Doug L. James, and Dinesh K. Pai. 2008. Staggered Projections for Frictional Contact in Multibody Systems. *ACM Trans. on Graph. (SIGGRAPH Asia)* 27, 5 (2008). Article No. 164.

Yang Liu, Hao Pan, John Snyder, Wenping Wang, and Baining Guo. 2013. Computing Self-Supporting Surfaces by Regular Triangulation. *ACM Trans. on Graph. (SIGGRAPH)* 32, 4 (2013). Article No. 92.

Masaaki Miki, Takeo Igarashi, and Philippe Block. 2015. Parametric Self-supporting Surfaces via Direct Computation of Airy Stress Functions. *ACM Trans. on Graph. (SIGGRAPH)* 34, 4 (2015). Article No. 89.

Mohammad Mirkhalaf, Tao Zhou, and Francois Barthelat. 2018. Simultaneous Improvements of Strength and Toughness in Topologically Interlocked Ceramics. *Proceedings of the National Academy of Sciences of the United States of America* 115, 37 (2018), 9128–9133.

John Allen Ochsendorf. 2002. *Collapse of Masonry Structures.* Ph.D. Dissertation. Massachusetts Institute of Technology, Cambridge, Massachusetts, USA.

Daniele Panozzo, Philippe Block, and Olga Sorkine-Hornung. 2013. Designing Unreinforced Masonry Models. *ACM Trans. on Graph. (SIGGRAPH)* 32, 4 (2013). Article No. 91.

Nico Pietroni, Marco Tarini, Amir Vaxman, Daniele Panozzo, and Paolo Cignoni. 2017. Position-based Tensegrity Design. *ACM Trans. on Graph. (SIGGRAPH Asia)* 36, 6 (2017). Article No. 172.

Matthias Rippmann, Tom Van Mele, Mariana Popescu, Edyta Augustynowicz, Tomás Méndez Echenagucia, Cristián Calvo Barentin, Ursula Frick, and Philippe Block. 2016. The Armadillo Vault: Computational design and digital fabrication of a freeform stone shell. In *Advances in Architectural Geometry.* 344–363.

Stephan Schaare, Werner Riehemann, and Yuri Estrin. 2009. Damping Properties of an Assembly of Topologically Interlocked Cubes. *Materials Science and Engineering A* 521-522 (2009), 380–383.

Hijung V. Shin, Christopher F. Porst, Etienne Vouga, John Ochsendorf, and Frédo Durand. 2016. Reconciling Elastic and Equilibrium Methods for Static Analysis. *ACM Trans. on Graph.* 35, 2 (2016). Article No. 13.

Thomas Siegmund, Francois Barthelat, Raymond Cipra, Ed Habtour, and Jaret Riddick. 2016. Manufacture and Mechanics of Topologically Interlocked Material Assemblies. *Applied Mechanics Reviews* 68, 4 (2016), 040803:1–15.

Peng Song, Bailin Deng, Ziqi Wang, Zhichao Dong, Wei Li, Chi-Wing Fu, and Ligang Liu. 2016. CofiFab: Coarse-to-Fine Fabrication of Large 3D Objects. *ACM Trans. on Graph. (SIGGRAPH)* 35, 4 (2016). Article No. 45.

Peng Song, Chi-Wing Fu, and Daniel Cohen-Or. 2012. Recursive Interlocking Puzzles. *ACM Trans. on Graph. (SIGGRAPH Asia)* 31, 6 (2012). Article No. 128.

Peng Song, Chi-Wing Fu, Yueming Jin, Hongfei Xu, Ligang Liu, Pheng-Ann Heng, and Daniel Cohen-Or. 2017. Reconfigurable Interlocking Furniture. *ACM Trans. on Graph. (SIGGRAPH Asia)* 36, 6 (2017). Article No. 174.

Peng Song, Zhongqi Fu, Ligang Liu, and Chi-Wing Fu. 2015. Printing 3D Objects with Interlocking Parts. *Comp. Aided Geom. Des.* 35-36 (2015), 137–148.

Chengcheng Tang, Xiang Sun, Alexandra Gomes, Johannes Wallner, and Helmut Pottmann. 2014. Form-finding with Polyhedral Meshes Made Simple. *ACM Trans. on Graph. (SIGGRAPH)* 33, 4 (2014). Article No. 70.

Keke Tang, Peng Song, Xiaofei Wang, Bailin Deng, Chi-Wing Fu, and Ligang Liu. 2019. Computational Design of Steady 3D Dissection Puzzles. *Comp. Graph. Forum (Eurographics)* 38, 2 (2019), 291–303.

Oliver Tessmann. 2012. Topological Interlocking Assemblies. In *Physical Digitality: Proceedings of the 30th eCAADe Conference*, Vol. 2. 211–219.

M. F. Thorpe and P. M. Duxbury. 2002. *Rigidity Theory and Applications.* Kluwer Academic Publishers.

Irina Miodragovic Vella and Toni Kotnik. 2016. Geometric Versatility of Abeille Vault: A Stereotomic Topological Interlocking Assembly. In *Complexity & Simplicity: Proceedings of the 34th eCAADe Conference*, Vol. 2. 391–397.

Etienne Vouga, Mathias Höbinger, Johannes Wallner, and Helmut Pottmann. 2012. Design of Self-supporting Surfaces. *ACM Trans. on Graph. (SIGGRAPH)* 31, 4 (2012). Article No. 87.

Ziqi Wang, Peng Song, and Mark Pauly. 2018. DESIA: A General Framework for Designing Interlocking Assemblies. *ACM Trans. on Graph. (SIGGRAPH Asia)* 37, 6 (2018). Article No. 191.

Michael Weizmann, Oded Amir, and Yasha Jacob Grobman. 2016. Topological Interlocking in Buildings: A Case for the Design and Construction of Floors. *Automation in Construction* 72, 1 (2016), 18–25.

Michael Weizmann, Oded Amir, and Yasha Jacob Grobman. 2017. Topological Interlocking in Architecture: A New Design Method and Computational Tool for Designing Building Floors. *International Journal of Architectural Computing* 15, 2 (2017), 107–118.

Emily Whiting, John Ochsendorf, and Frédo Durand. 2009. Procedural Modeling of Structurally-Sound Masonry Buildings. *ACM Trans. Graph. (SIGGRAPH Asia)* 28, 5 (2009). Article 112.

Emily Whiting, Hijung Shin, Robert Wang, John Ochsendorf, and Frédo Durand. 2012. Structural Optimization of 3D Masonry Buildings. *ACM Trans. Graph. (SIGGRAPH Asia)* 31, 6 (2012). Article 159.

Randall H. Wilson and Toshihiro Matsui. 1992. Partitioning an Assembly for Infinitesimal Motions in Translation and Rotation. In *IEEE/RSJ Intl. Conf. on Intelligent Robots and Systems.* 1311–1318.

Shi-Qing Xin, Chi-Fu Lai, Chi-Wing Fu, Tien-Tsin Wong, Ying He, and Daniel Cohen-Or. 2011. Making Burr Puzzles from 3D Models. *ACM Trans. on Graph. (SIGGRAPH)* 30, 4 (2011). Article No. 97.

Jiaxian Yao, Danny M. Kaufman, Yotam Gingold, and Maneesh Agrawala. 2017b. Interactive Design and Stability Analysis of Decorative Joinery for Furniture. *ACM Trans. on Graph.* 36, 2 (2017). Article No. 20.

Miaojun Yao, Zhili Chen, Weiwei Xu, and Huamin Wang. 2017a. Modeling, Evaluation and Optimization of Interlocking Shell Pieces. *Comp. Graph. Forum* 36, 7 (2017), 1–13.

Jennifer Furstenau Zessin. 2012. *Collapse Analysis of Unreinforced Masonry Domes and Curving Walls.* Ph.D. Dissertation. Massachusetts Institute of Technology, Cambridge, Massachusetts, USA.

Yinan Zhang and Devin Balkcom. 2016. Interlocking Structure Assembly with Voxels. In *IEEE/RSJ Intl. Conf. on Intelligent Robots and Systems.* 2173–2180.